Flow and contaminant transfer at the interface of an aerodynamic containment barrier subjected to the wake of a moving obstacle

Emmanuel Belut, Sullivan Lechêne, Benoît Trouette, Stéphane Vincent, Georges Halim Atallah

Flow and contaminant transfer at the interface of an aerodynamic containment barrier subjected to the wake of a moving obstacle

Emmanuel Belut[a], Sullivan Lechêne[a], Benoît Trouette[b], Stéphane Vincent[b], Georges Halim Atallah[b]

[a] *INRS, 1 rue du Morvan, Vandoeuvre, F-54500, France*
[b] *Universite Gustave Eiffel, Universite Paris Est Creteil, CNRS, UMR 8208, MSME, Marne-la-Vallee, F-77454, France*

Abstract

This contribution is an experimental and numerical study on the breach of a containment barrier subject to the transient wake of a moving obstacle. In the context of a 100 m^3 laboratory with high air exchange rate (8.5 h^{-1}), a passive gaseous contaminant is emitted at a controlled flow rate from the bottom surface of an open cavity (0.8×0.34 m^2 wide). Starting from a steady and turbulent airflow situation, a human-sized obstacle passes in front of the cavity and disturbs the established flow. The containment breach is then analysed by recording gas concentrations and velocity components, measured at the cavity open surface, with photoionization detectors and 2D3C PIV, respectively. A penalty method coupled with LES is used to model the experimental setup and predictions are compared to measurements. The numerical model is found to be able to reproduce the contaminant concentrations, air velocities and main POD modes of the flow within experimental inaccuracies. This modelling approach appears to be suitable to study, in-silico, the effect of drafts induced by human motion on aerodynamic barriers. CFD results also show that the levels of pollutant leaks are intrinsically dependent on the ventilation conditions. Up to 100% variation of contaminant concentration peaks can be observed, depending on the initial turbulent state of the room.

Keywords: contaminant transport, wake, LES, PIV, POD, immersed boundary

Table of symbols

W Obstacle cross-stream dimension (width)
U_{ref} Typical convective velocity in the room in steady-state
U_{obj} Obstacle nominal velocity (1 m.s^{-1})
u, v, w Instantaneous velocity components
$\mathbf{u}$ Velocity vector
Re_R Room Reynolds number
Re_C Cavity Reynolds number
Re_W Moving obstacle Reynolds number
τ_p Local mean age of air at point p
k Coverage factor for uncertainty expansion
$\langle\rangle$ Phase-averaging operator
V Room volume
Ri_{ij} Richardson number between positions i and j
C, $\widetilde{C}$ Acetone concentration and measured (filtered) concentration
Q Fresh air volume flow rate
T_L Air renewal integral time scale
T_T Moving obstacle transit time
T_s Typical obstacle vortex shedding period
Str Obstacle Strouhal number
u_k k^{th} Velocity component
D Data matrix
K Temporal auto-correlation matrix of the dataset
Λ_P Eigenvalues matrix of K
Σ_P Amplitude matrix of POD modes
Φ_P Basis matrix of spatial POD modes
Ψ_P Temporal basis matrix of POD modes.

1. Introduction

It is a truism to say that an efficient ventilation is required to achieve good air quality in all types of built environments. Traditionally, building ventilation has been designed with a steady state performance objective, disregarding transient effects. However, it quickly became apparent that air flows and contaminant transfers were largely affected by transient phenomena related to human activity [19, 29]. It is necessary to take into account human and object movements, door opening and crossing, etc. in the design of ventilation systems. This is particularly the case for environments where the containment of airborne pollutants is ensured by ventilation (fume cupboards [22, 41, 47], operating rooms [5, 48], isolation rooms [14, 21, 38, 43, 49], clean rooms [42], etc.). Studies of the distruptive movement effects on the dynamics of indoor air flow and airborne pollutants have considerably developed in the last decade, especially with increasing detailed CFD studies. Early numerical studies were mainly focued on the wake of a humanoid body translating in an infinite space [15, 31]. However, the transient aspect of the movement and the wall-bounded character of the rooms were not considered. The effect of the movement (people, doors, etc.) on indoor air flows was firstly introduced in stationary regime. Distributed momentum sources were used to represent the average mixing effect induced by the movement of people [5]. The unsteady regime was addressed in a second step and the effect of a mobile geometry on the flow was introduced thanks to the dynamic mesh technique [1, 2, 9, 8, 12, 18, 20, 21, 26, 35, 43, 45, 49, 50]. Currently, the immersed boundary method [34, 38] is well established and permits accurate geometrical representations of the moving objects, even for complex trajectories [10, 11].

Despite these numerical developments and progesses, full-scale experimental reference data are still rare [9, 21, 52]. It is necessary to reach satisfactory spatial and temporal resolution on the measurements in order to validate numerical models. To the authors knowledge, the most complete up to date study is Poussou et al. [35], Poussou and Plesniak [36], who experimentally characterized by planar-PIV and PLIF measurements the dispersion of a pollutant in the wake of an obstacle. The experimental setup was a reduced water model, and the objective was to represent the effect of a person moving in an airliner cabin. However, the PLIF technique used to measure the pollutant concentration was only qualitative due to the non-linear fluorescent response of the dye used. It was found very challenging to ensure the

dynamics similarity of the full scale problem [30, 46].

In a ventilated cabin, Bjørn and Nielsen [4] studied the dispersion of a tracer gas emanated from a manikin in either a sitting or a standing position (with back and forth movements). However, only time-averaged concentration data were extracted and no characterization of the airflow velocity field was conducted. Matsumoto and Ohba [28] studied experimentally the influence of a moving object on air distribution in displacement ventilated rooms, but only from a time-averaged point of view. With tracer gas measurements, Brohus et al. [6] also investigated the influence of human subjects movements on the ventilation effectiveness. Once again, this experiment was not designed to validate CFD model since it lacks many essential features (repeatability of motion, airflow characterization, boundary control). In the context of a water scaled model, Eames et al. [14] measured experimentally, by means of optical analysis of dye spreading, the flow rate exchanged between two rooms during door openings. Although this case provides useful data for model validation, it lacks a detailed characterization of the velocity field and of the initial and boundary conditions (both velocity and concentration fields) to form a validation case for CFD. Moreover, similarity issues exist [46] to extrapolate this experiment to the 1:1 scale situation (especially concerning the time schedule for door opening).

With one-component hot wires anemometers, Han et al. [20] measured the time evolution of air velocity in the wake of a manikin translating in a corridor.Assuming components decorrelation, they reconstructed the 3 velocity components by repeating the measurements and the orientation of anemometers. This approach is necessarily approximate, considering the highly turbulent 3D structure of the wake, the intrusiveness of anemometers, their sensitivity to velocity orientation, and their measurement range. Moreover, this study does not address the problem of a simultaneous transport of pollutants and does not detail the initial and boundary conditions of the flow.

Saarinen et al. [38] measured with a gas tracing technique the total volumes of air exchanged between an isolation chamber and its antechamber. They considered the case of a separation door, with or without the passage of a manikin and subject to various ventilation configurations. In addition, they used smoke visualization to illustrate qualitatively the transfer. The net volume exchanged between the rooms is a useful validation data for the numerical simulations. Unfortunately, no detailed spatial and temporal characterization of the transient transfer was given. This remark also applies

to Chang et al. [9] who measured, without ventilation and with tracer gas, the total air volume exchanged during a door opening subject to an initial pressure difference of 30 Pa.

Luo et al. [26] measured by planar PIV the air flow distributions in the wake of an elliptic cylinder and of a down-scaled moving manikin in a water model of a corridor. A good spatial and temporal resolution of velocity data is provided by the experiment, which makes it suitable for CFD validation. However, the similarity parameters used in the experiment can not be extrapolated to a real scale situation [36, 46]. Also, only the flow velocity field is studied, without the pollutant tranfert nor the ventilation interactions.

Using ultrasonic anemometry with high temporal (4 Hz) and spatial accuracy (20 points), Bhattacharya et al. [3] measured the 3 instantaneous air velocity components along the wake of a moving person in a ventilated room. The study was not intended for CFD model validation. The use of a human subject does not guarantee the repeatability of the movement in between successive tests. Moreover, the airborne pollutant transfer is disregarded and the human movement was not clearly characterized. Rouaud et al. [37] has experimentally studied the effect of external perturbations (door opening) on the containment of a scaled-down minienvironment. The transient containment breach is qualified by 2D laser tomography and by real time (500 Hz) measurement of a tracer gas concentration. Regarding the disturbance of the air velocity field in the transient regime, the validation data for a CFD modeling are reduced to their qualitative aspect (laser visualization) as the use of planar PIV was reserved only for the initial state.

Goldasteh et al. [18] measured time-resolved particulate resuspension rate induced by the motion of a single shoe on the floor. However, no velocity measurements were provided and the apparatus was not dedicated to pollutant transfer at room scale. In ventilated operating configuration, Villafruela et al. [48] measured at 24 spatial locations and at a 10 Hz frequency, the time evolution of the 3 instantaneous air velocity components in a cross section facing an opening sliding door. Cases with and without human traffic were considered. This test case is not perfectly suitable either for CFD model validation since the door kinematics and the person motion are not detailled. Futhermore, a precise description of the initial and the boundary conditions of the airflow are missing. Shao et al. [42] studied experimentally the transfer of airborne particles through the doorway of a cleanroom due to the movement of a person. However, the number of concentration sampling points is limited and no airflow characterization was performed. The initial

flow conditions are also difficult to conceive because of very complex handling of the ventilation (heaters are stopped before door opening and the air circuit is modified through the closing of bypass ducts). Overall, this case is also not suitable for CFD validation.

Lv et al. [27] performed point measurement of velocity magnitude and tracer gas concentration in the context of a range hood flow disturbed by the wake of a human walking. However, the spatial and temporal resolution used is limited for CFD validation (resp. 4 and 5 points in the room for concentration and velocity magnitude, and acquisition rate of 30 s and 5 s for concentration and velocity, respectively). Moreover, a volunteer performed the human motion, which leads to a loss of motion control and repeatability. Opened windows and doors also lead to a lack of precision for the boundary and initial conditions of the experiment.

To summarize, there is a lack of reference experimental data to validate CFD models capable of predicting the effect of moving objects (obstacle, door or person) on the transient dispersion of pollutants indoor. Most of the referenced experiments present at least one of the following drawback: 1) a lack of control or detail regarding the description of boundary or initial conditions (we will detail the importance of this aspect in the paper), 2) a spatial or temporal resolution of measurements being too coarse to be comparable to CFD, 3) limits in the similarity with real scale problems. In addition, beyond the experimental limits of the referenced studies, none considers the transient rupture of the containment of a ventilated enclosure induced by the wake of a moving obstacle. This specific aspect represents many important issues for safety of people [22, 41, 47].

Finally, from a CFD modeling point of view, most of the previously referenced studies prefer the URANS k-ϵ RNG turbulence model associated with the dynamic mesh technique. However, it is widely recognized that large eddy simulation (LES) performs much better than RANS for complex indoor airflows [51] in the presence of bluff-body wakes.

Moreover, dynamic meshes are known to be cumbersome to generate and are associated to a high computational cost [52]. On another side, the family of immersed boundary methods allows a realistic descrption of the geometry at a reduced computational cost [10]. Even if partial validations are proposed [10, 38], this approach has not been subject to a detailed experimental validation in the case of contaminant transfer induced by the wake of mobile objects. We can also observe that the validation of CFD models in previous

works is generally based on qualitative comparisons of velocity or pressure fields [26, 35, 49, 50], or point-to-point comparisons [27, 34, 52], whereas tools for comparing the dynamic content of flows by model reduction (like POD [25, 44]) are now commonly used.

In this context, the objectives of this article are multiple:

- to propose a scale 1 experimental case for the validation of CFD models dedicated to the simulation of indoor airborne contaminant transport induced by mobile objects. Room ventilation and the aerodynamic containment barrier will be taken into account.
- to evaluate the ability of a combined LES and a penalty-based approach to predict the contaminant transfer occurring at the interface of a containment barrier submitted to the transient wake of a moving obstacle.
- to illustrate the impact of the initial airflow condition on the dispersion of pollutants induced by the movement of objects. To our knowledge, this aspect is not addressed in previous studies.
- to promote POD as a tool to analyse and compare the measured and simulated airflows. This approach allows a more relevant analysis with respect to the point-to-point comparison methods.

A scale 1 experimental case is set up to reach these goals. For immediate application, this case has the advantage to faithfully reproduce the european standardized robustness test of fume cupboards [7]. After presenting an overview of the test case, the paper describes its experimental realization, with associated instrumentation and measurement techniques. Supplementary materials are used when extensive details are believed necessary. The physical model tested is then detailed together with its numerical implementation and resolution procedure. Numerical and experimental results are then compared in a dedicated section and the consistency of comparisons is discussed. Throughout this paper, unless otherwise specified, measured values are written $(y \pm U_y)$ where U_y is the expanded uncertainty on y with a coverage factor equal to 2.

2. Material and methods

2.1. Case overview

An overview of the test case is sketched in Figure 1, with the coordinate system used in the paper. It consists of a 6.7 × 4.5 × 3.5 m^3 room in which an open 0.8 × 0.34 × 0.4 m^3 (width × height × depth) cavity is placed. Temperature-controlled air is supplied in the room at a constant flow rate of 0.25 $m^3.s^{-1}$, by means of a low velocity diffuser (∼0.2 $m.s^{-1}$) placed along a vertical corner, and air is extracted partly (44%) through the rear face of the open cavity, the remaining 56% being extracted through a circular opening in the ceiling.

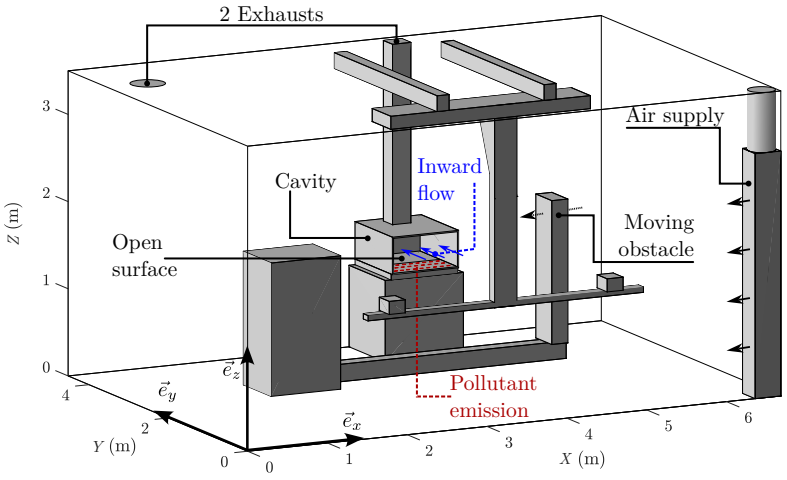

Figure 1: overview of the studied configuration

Detailed dimensions and technical drawings and CAD models are provided as supplementary material. The room contains various obstacles necessary for instrumentation that are described later on. The open cavity mimics a very simplified open fume hood with frontal velocity of 0.4 $m.s^{-1}$. It is placed on a rectangular support so that its bottom surface is about at table height (1.08 m). The back face of the open cavity is a perforated metal grid, behind which a 0.8 × 0.4 × 0.4 m^3 plenum is placed, aiming at making uniform the drawn airflow. Air is further extracted through the plenum by a vertical square duct leading to the air extraction system. The outermost part of the bottom surface of the cavity is a diffusing surface (0.76 × 0.165 m^2) through which a controlled mass flow rate of a mixture of air and tracer gas is

	room temperature (°C)	air density (kg.m^{-3})	supplied air flow rate Q (m^3.s^{-1})	cavity extracted flow rate (m^3.s^{-1})	2nd extraction flow rate (m^3.s^{-1})
campaign 1 : tracer gas	(21.2 ± 1.2)	$(1.15 \pm 1.3\%)$	$(0.249 \pm 1.4\%)$	$(0.111 \pm 4.9\%)$	$(0.139 \pm 3.1\%)$
campaign 2 : PIV	(20.9 ± 1.3)	$(1.14 \pm 1.3\%)$	$(0.25 \pm 1.4\%)$	$(0.0994 \pm 6.3\%)$	$(0.134 \pm 3.4\%)$

Table 1: Operating mean experimental parameters with expanded uncertainties

emitted at a low velocity (0.01 m.s^{-1}), to mimic the continuous emission of a pollutant from the working area of a fume hood. An obstacle of approximate human dimensions ($1.65 \times 0.4 \times 0.2$ m^3 parallelepiped) is placed in front of the cavity, with its basis fixed on a remote-controlled traverse system laid on the ground. The obstacle is then able to translate on demand in the direction parallel to the open surface of the cavity. A single stride of 2.66 m, at a normal distance from the open surface of 0.4 m and at a nominal velocity $U_{obj} = 1$ m.s^{-1} is used as reference movement. The flow chart of the studied time-dependent mass and momentum transfer can be summarized as follows: the obstacle is initially motionless, at the right end of the traverse as sketched on Figure 1. The airflow in the room reaches an initial statistically steady but turbulent flow regime (typical Reynolds numbers are $Re_R = 6 \times 10^4$ for the room and $Re_C = 1 \times 10^4$ for the cavity), and the tracer gas emitted in the cavity is entirely sucked in through the back face of the cavity. Starting from this initial condition, the moving obstacle makes a single stride in front of the cavity, with a width-based Reynolds number of the obstacle $Re_W = 3 \times 10^4$: the wake of the obstacle disturbs the flow initially established, until the flow reaches back a new statistically steady regime. We study here the flow and pollutant transfer that occur during the transient phase. In particular, we wish to characterize the containment breach that occurs when the air velocities become reversed at the open surface of the cavity and when the tracer gas escapes from the confined volume bounded by the cavity. The whole air volume in the room is the system of interest, meaning that no interference from outside the room must occur during experimental time; all controls are then placed outside and the door remains closed during the time needed. The main operating parameters of the case are given in table 1.

2.2. Experimental

2.2.1. Boundary condition controls and characterization

Controls of heat and VOC transfer. A series of controls is deployed to prevent natural convection from ruling the airflow in the room, and to limit the background concentration of airborne Volatile Organic Compound (VOC), since a VOC is used as a tracer gas. The walls of the room are made up of airtight sandwich panels filled with polyurethane foam, of thickness 60 mm, thermal resistance 15 $m^2.K.W^{-1}$, while the roof is of identical composition with thickness 80 mm and thermal resistance 20 $m^2.K.W^{-1}$ (SI60 and LG80 panels, Dagard SAS, Boussac, France). Panels are certified as low Volatile Organic Compound (VOC) emitters according to French classification (A+ class). The floor of the room is a painted concrete slab under which there is a heated basement at ambient temperature. The room is located in a test hall so that none of its sides is in contact with an external wall of the hall, and the hall is maintained at ambient temperature. The temperature of air in the hall, outside the room, is continuously monitored on two points located on the largest walls of the room at a height of 1.8 m. The temperature of air supplied in the cabin is adjusted to that of the hall to prevent temperature gradients through the walls. The temperature of air exhausted by the two outlets is also continuously measured. At last, a vertical Z profile equipped with 10 evenly spaced thermocouples is placed in the room at $X = 1.77$ m, $Y = 2.32$ m to evaluate the temperature homogeneity in the room. All thermocouples are Almemo Cu-CuNi type T model ZA9000-FST thermocouples, connected to an Almemo 5690-2 logger (Ahlborn, Holzkirchen, Germany).They are intercompared before the experiment. For tracer gas experiments, the concentration of airborne VOCs in the supplied air and in the exhausted air are continuously measured by means of Photoionization detectors (PID) (Mini PID AH, 10.6 eV UV lamp, ION Science LTD, England). Calibration details are given in supplementary S.**??**. The position of the evoked thermocouples and PIDs are given in supplementary with an overview of the room in the test hall.

The dispersion across experiments of temperature differences measured between the thermocouples in the room is reported in supplementary S.**??**, for steady state initial conditions. It appears that 99% of temperature differences are below 1°C with an average of 0.35°C, indicating a good but imperfect temperature control. The relative influence of natural convection over forced convection induced by ventilation is examined by considering the distribution

of signed Richardson numbers Ri_{ij} between pairs of thermocouples i and j of the vertical profile evoked previously, with $Ri_{ij}(t) = \frac{g\beta\Delta T_{ij}(t)\Delta z_{ij}}{U_{ref}^2}$ (where g is the gravitational acceleration, β is the thermal expansion coefficient, Δz_{ij} is the relative height difference $z_i - z_j$ between thermocouples i and j, and U_{ref} is the typical convective velocity in the room induced by ventilation, taken as $U_{ref} = 0.2$ m.s^{-1} which corresponds to the bulk velocity at the air diffuser surface). Note that according to the definition of Ri_{ij}, only negative values are likely to lead to natural convection because of negative temperature vertical gradient. We observe that all absolute values of Ri_{ij} are below 1: this indicates that the flow in the room in steady-state conditions is globally dominated by the forced convection induced by ventilation. However, 39% of Ri_{ij} are in the range $[-0.1, -1]$ and 11% are in the range $[-0.5, -1]$, which means that some uncontrolled natural convection may influence the steady-state flow and induce some variability of the initial flow conditions for the time-dependent problem. For the time-dependent problem where the typical convective velocity in the room is $U_{obj} = 1$ m.s^{-1}, Ri_{ij} numbers become much smaller than 1 and thus natural convection is marginal.

Airflow controls and measurements. The air supplied in the cabin is taken in the upper part of the hall, passes through a HVAC system and then through an airtight pipe with a straight length of 6 m, diameter 0.2 m laying on the roof of the room, before being introduced in the air diffuser. In this straight length, a calibrated venturi flow meter (Preso PCVL1E1A1, Badger Meter GmbH, Neuffen, Germany) is placed with an upstream length of 3.4 m and a downstream length of 2 m to ensure less than 0.7% uncertainty on their discharge coefficient according to [32]. Similarly, each air exhaust is connected to a straight airtight pipe (length 6 m, diameter 0.2 m) laid on the roof of the room, in which the same model of venturi flow meter is placed at suitable position. These pipes are further connected to independent extraction fans on the top of the building. Each venturi flow meter was independently calibrated by a COFRAC-accredited laboratory (CETIAT, Villeurbanne, France). Pressure drops at the venturi are measured continuously by means of Almemo FD A602S1K high frequency manometers linked to an Almemo 2690 logger (Ahlborn, Holzkirchen, Germany). To provide suitable inputs for the CFD modelling of the room, the 3 components of air velocity at the surface of the air diffuser are measured prior to experiments by means of a 3D ultrasonic anemometer (KAIJO WA-390, Sonic corp., Tokyo, Japan). Measurements are performed over 351 evenly spaced points at a nor-

mal distance of 6 cm with respect to the two faces of the air diffuser. For each point, the instantaneous velocity is acquired with a time resolution of 0.1 s during 10 s. Mean velocity and temporal standard deviation are extracted, providing an estimate of turbulent kinetic energy. To assess the repeatability of this flow condition at the diffuser, velocity measurements were repeated twice more for a subset of 49 points of the 351 points. Less than 0.045 $\mathrm{m.s^{-1}}$ variation of velocity magnitude across repetitions was found for 95% of measurement points (i.e. 10% of the diffuser peak velocity) indicating a good control of the flow boundary condition. Measurement details and velocity profile data are given in supplementary S.**??**.

Tracer gas emission from the diffusing surface of the cavity. A mixture of air with a concentration of acetone vapors of (2150 ± 13) ppm is used as a tracer gas. It is generated by means of an evaporator cell with mass-flow controllers for air and acetone (CEMLab system, Bronkhorst High-Tech B.V., Netherlands). The mixture is led through a non adsorbent PTFE tube to a home made diffuser placed on the bottom surface of the open cavity. The tracer gas is released through a surface of 0.768×0.168 $\mathrm{m^2}$ consisting of a metal diffusing cloth with 80 µm holes. A total volume flow rate of mixture of (111.7 ± 0.55) $\mathrm{l.min^{-1}}$ at room temperature is used so as to obtain a bulk velocity at the diffuser's surface of 0.015 $\mathrm{m.s^{-1}}$, i.e. which is marginal with respect to that of the ingoing airflow (0.4 $\mathrm{m.s^{-1}}$). Standard uncertainties on generation parameters are obtained from the manufacturer's specifications. Information regarding the conception of the diffuser are given in supplementary S.**??**.

Characterization of the obstacle motion. The motion of the moving obstacle (time-resolved position and velocity) was measured by means of a wire position sensor (MEIRI, model WS17KT-6250-R1K-L10, SPHEREL Systems, Portet sur Garonne, France). The obtained characteristics are provided in supplementary S.**??**.

2.2.2. Initial condition characterization and repeatability

Initial conditions are key determinants of the studied time dependent problem. The characterization of these initial conditions and of their repeatability was performed as follows. The initial state of the flow in the room is the statistically steady-state turbulent flow regime reached when the obstacle is motionless at its initial position and when all boundary conditions are in the steady state previously exposed. The initial flow state in

PID#	221	222	223	231	232	233
coordinates (m)	(3.34, 2.26, 0.88)	(3.34, 2.26, 1.75)	(3.34, 2.26, 2.63)	(3.34, 3.4, 0.88)	(3.34, 3.4, 1.75)	(3.34, 3.4, 2.63)
τ_p (s)	(453 ± 12)	(475 ± 12)	(575 ± 25)	(431 ± 12)	(420 ± 13)	(513 ± 29)

Table 2: Measured mean ages of air in initial conditions, with expanded uncertainties

the room and its repeatability were characterized by the moments of concentration histories obtained when filling/emptying the room with a tracer gas, using the local mean age of air concept [40]. The step-up/step down methods were retained for this characterization: on demand, a tracer gas consisting of air saturated with acetone vapors was injected at a controlled flow rate of $(0.461 \pm 0.65\%)$ Nl.min^{-1} in the duct supplying air in the room, at an upstream distance of 42 times the duct diameter to ensure perfect mixing of the tracer gas with the supplied air. A first PID was placed at the surface of the inlet air diffuser, to detect the time at which the step-up or step-down of tracer gas injection arrived in the room. A series of 6 similar PIDs were placed as shown in supplementary figure S.**??** and time series of acetone concentrations at the PIDs were recorded during 16 repetitions of filling/emptying of the room with the tracer gas. The repetitions of the trials were distributed over 4 days with 4 step-up/step-down per day. All PIDs, including the one at inlet, were connected to the same logger (GL820, Graphtec Corporation, Yokohama, Japan) to ensure time synchronization. From the time series of concentrations, 32 measurements of mean ages of air τ_p per PID position were then computed following the procedure exposed in supplementary S.**??**, i.e. 16 for step-up and 16 for step-down. Table 2 reports mean τ_p values and associated expanded uncertainties. For all 6 measurement points, the expanded uncertainties of τ_p are between 2.4% and 5.7% of τ_p, indicating an appreciable control of initial flow conditions in the room. Measured τ_p are also plotted on figure 3 together with corresponding CFD results for comparison purposes, see section 3.1.

2.2.3. Measurement instruments

Time resolved 2D3C-PIV at the open surface of the cavity. The three instantaneous velocity components are measured in the plane of the open surface by a stereo (i.e. 2D-3C) PIV system (Dantec Dynamics A/S, Skovlunde, Denmark). Images are acquired at a frequency of 5 Hz by two HiSense Zyla 5.5 MP cameras in translation configuration with Scheimpflug arrangement and the laser sheet is generated by a 532 nm-120 mJ Nd:YAG laser. The

overall layout is sketched on supplementary figure S.?? . The thickness of the laser sheet is set at 8 mm in order to limit the seeding losses in the direction normal to the laser sheet (main flow direction). The sheet is positioned at 2 mm from the open surface of the chamber to avoid reflections. The calibration of the system, the acquisition and the processing of the images are carried out with the software DynamicStudio 7.4 (Dantec Dynamics A/S, Skovlunde, Denmark). The calibration is performed via a planar 0.8×0.345 m^2 calibration plate, using a 3D reconstruction model (polynomial of order 3 for the two in-plane components and order 2 for the normal component), built on 7 calibration planes positions. The average retroprojection error of the calibration pattern after calibration is 0.4 pixel.

The seeding of the medium is performed by a helium-filled soap bubble generator (HFSB, LaVision GmbH, Göttingen, Germany) via two diffusing wings each containing 20 injection nozzles. The two wings are placed about 1 m above the ground nearby the inlet air diffuser and positioned at about 90° to each other. The bubbles have an average diameter of 300 µm (manufacturer specifications).

The capture of the image sequence is triggered automatically by a switch when the moving obstacle has travelled (35.3 ± 0.5) cm from its initial position, which corresponds to a time delay with respect to the start of the obstacle motion of (0.52 ± 0.03) s. Then 100 images are recorded at 5 Hz, i.e the total measurement time is from $t = 0.52$ to $t = 20.32$ s after the obstacle has started.

Once acquired, the analysis synoptic of the image sequence is as follows. First, images partly obstructed by the obstacle are removed from the sequence, which corresponds to 9 images between $t = 0.6$ s and $t = 2.2$ s. Then, the mean image of the sequence is subtracted to remove the residual background, and the low frequency spatial illumination gradient is also removed by image filtering (smoothed local minimum of each 16×16 pixel neighborhood). A low pass filter with cut-off length of 1 pixel is applied to remove camera noise and to keep only the images of the seeding particles. Finally, residual reflections are manually masked. The following PIV analysis is then applied. Adaptative 2D correlation with interrogation window shift is performed for each stereo view, with decreasing window sizes from 256×256 to 64×64, with a window overlap of 50%. The average diameter of seeding particle images is 2.5 pixels and the final average seeding density is of 90 particles per 64×64 window on the left view and of 50 particles per 64×64 window for the right view. No window deformation with velocity gradients

was found necessary. The time interval between images was set to 1.8 ms: the corresponding average particle displacement between frames was then in the range $[2, 5]$ pixels, depending on time, with 95% of displacements between 0.5 and 3.3 pixels. The obtained 2D vector fields are then interpolated and dewarped according to the calibration model to yield the 3 components of velocity on the open face of the cavity.

The experiment is repeated 20 times and phase-averaged time-resolved velocity fields are hence computed.

Velocity measurement uncertainties are estimated by two indirect methods. First, the uncertainty on the displacement of seeding particles is evaluated by imposing a known translation to a dotted target, by means of a 3D traverse system (ISEL, Eiterfeld , Germany). The average difference relative to the imposed displacement was 1.6% for the component normal to the measurement plane and 1.4% for the two in-plane components. Details of this evaluation are provided in supplementary S.**??**. This difference is assumed to correspond to the ideal uncertainty of the measurement system linked to optical calibration and stereo-reconstruction, disregarding PIV uncertainties due to particle losses, laser cavity misalignment, space-varying illumination etc. In real shooting condition, the velocity measurement uncertainty can be estimated by comparing the flow rate measured by the venturi flowmeter with the result obtained by integrating the PIV velocity field. The PIV-integrated flow rate was found systematically lower than the actual venturi-measured flow rate, with a difference ranging between 6.8 and 9.8% depending on the experiment. This discrepancy is believed to better represent the PIV systematic uncertainty on the Y-velocity component in real shooting conditions. Details of this evaluation are also provided in S.**??**.

Time resolved gas concentration measurements. The same PID than those used to determine the mean ages of air in the room were employed to measure the time series of acetone concentration on 4 selected points of the open surface of the cavity for the time-dependent problem. Measurements were segregated from PIV measurements considering the verified repeatability of the experiment and the optical obstruction linked to the PID positioning. PID were mounted with their detecting orifice placed on the plane delimited by the open surface of the cavity, at a distance of 5 cm inward from the sides of the open cavity, as sketched on supplementary figure S.**??**. A light structure shown in figure S.**??** is used to place the PIDs with minimum intrusiveness. PIDs were found to need an individual in-situ calibration after warm-up,

hence the following calibration protocol was used. PIDs were switched on at least 30 minutes before experiments. After warm up, they were exposed to a mixture of dry air and isobutylene, generated by two mass flow controller and a standard isobutylene cylinder (Airliquide, Mitry-Mory, France). The calibration mixture was blown on the installed PIDs through PTFE tubings terminated by a cap enveloping the PIDs. Alternating isobutylene concentrations of 0 and (10.0 ± 0.22) ppm were used to determine the baseline and the slope of each PID response with respect to isobutylene concentration: 2-points calibration of the linear response of PID tension with isobutylene concentration was obtained by composing the average high and low tension levels of the PIDs, before and after every series of experiments. In practice, this PID calibration was repeated every 2 to 4 strides of the moving obstacle. Uncertainties on the average calibration coefficient were obtained by propagating random errors due to PIDs tension fluctuations during calibration and uncertainties on calibration mixture concentration. The calibration procedure is further documented in supplementary S.**??**. In the end, this calibration provides equivalent-isobutylene concentrations: this concentration is further converted into acetone concentration by considering an ionization conversion factor of 1, in accordance with the results of a comparison of the response of PIDs to these two gases carried out in the laboratory.

This in-situ calibration accounts for the baseline and gain of the PIDs response; however, PIDs also present a non-ideal dynamic response that must be evaluated to compare concentration measurements to simulations. Further on, we then denote C the true acetone concentration and $\widetilde{C}$ the concentration effectively measured by the PID (or filtered concentration), so that $\widetilde{C}(t) = C(t) * H(t)$ where $H(t)$ is the transfer function of the PID that accounts for its non-ideal response, and $*$ denotes the convolution product. The evaluation of the dynamic response of PIDs and the determination of their time-filtering transfer function was performed on a separate setup described in supplementary **??**, where PIDs were exposed to controlled square signals of isobutylene concentrations. This separate evaluation showed that the PIDs response could be approximated by an equivalent 2 pole transfer function with a 3 db cut-off frequency at 0.73 Hz that reads:

$$H(s) = \frac{0.903s + 0.132}{s^2 + 1.18s + 0.136}, \tag{1}$$

where s is the Laplace variable. The system identification was performed with

MATLAB and System Identification Toolbox (Release 2017a, The MathWorks, Inc., Natick, Massachusetts, United States), using an algorithm derived from [13]. For this model fit, the determination coefficient is $R^2 = 0.991$.

2.2.4. Time scales and dimensionless numbers

The studied flow is characterized by three main time scales: T_L, the typical integral time scale of air renewal in the room, defined as $T_L = V/Q$ for such a mixing ventilation situation, where V is the room volume and Q is the volume flow rate of fresh air supplied. Here, with $T_L = 422$ s, T_L is very close to the measured τ_p in the room in steady state (table 2) which confirms a mixing ventilation configuration. The second time scale for the time-dependent problem is T_T, the transit time of the moving obstacle, with $T_T = 2.88$ s. Since $T_T \ll T_L$, air renewal in the room is a quasi-static process with respect to the time-dependent problem. The third time scale is the typical vortex shedding period T_s induced by the moving obstacle. The obstacle is characterized by a minor to major axis ratio of 0.5 and a Reynolds number $Re_W = 2.6 \times 10^4$, based on its cross-stream dimension W and nominal velocity U_{obj}. For a comparable situation, [24] measured a Strouhal number over a rectangular cylinder $Str = \frac{W}{U_{obj} T_s} = 0.14$, from which we may estimate in the present case $T_s = 2.86$ s. Since $T_s \approx T_T$, the obstacle is expected to shed a single vortex during its stride.

The flow regime in the room is always turbulent, it is characterised by 3 main Reynolds numbers: $Re_W = 2.6 \times 10^4$ for the moving obstacle, $Re_c = 1.2 \times 10^4$ based on the hydraulic diameter of the cavity, and $Re_R = 6 \times 10^4$ for the room flow regime in steady-state, based on typical length $V^{\frac{1}{3}}$ and typical convective velocity in the room $U_{ref} = 0.2$ m.s^{-1} in steady-state.

Regarding the transport of the tracer gas, it is largely dominated by convection with a Péclet number of the order of the Reynolds number, since the Schmidt number of diluted acetone vapors in air is of 1.42 in operating conditions [16].

2.2.5. Experimental schedule

The experimental schedule is summarized by the chart of figure 2. In particular, it relies on the respect of a relaxation time $5T_L$ between successive experiments to ensure the repeatability of initial flow condition in the room, which corresponds to the flow in steady-state.

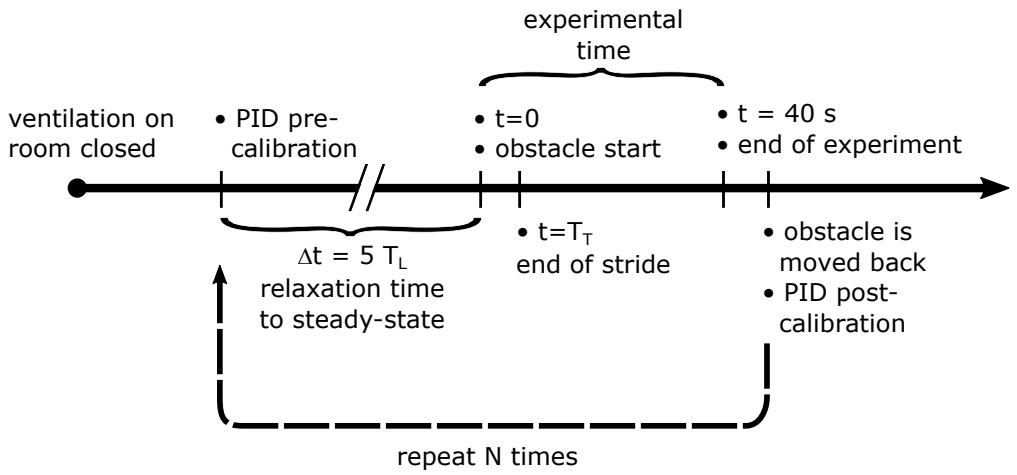

Figure 2: Experimental flow chart

2.3. Modelling

2.3.1. Models and numerical methods

Fluid flow is modelled by the classical isothermal and incompressible Navier-Stokes equations. The isothermal nature of the flow is justified by the estimation of Richardson numbers (see Sec. 2.2.1). Considering a turbulence modelling approach, the penalized Navier-Stokes equations for a Newtonian fluid, dry air in the present context, read:

$$\begin{cases} \nabla \cdot \mathbf{u} = 0 \\ \rho \left(\dfrac{\partial \mathbf{u}}{\partial t} + \nabla \cdot (\mathbf{u} \otimes \mathbf{u}) \right) = -\nabla p + \nabla \cdot \left((\mu + \mu_{sm}) \left(\nabla \mathbf{u} + (\nabla \mathbf{u})^{\intercal} \right) \right) + \mathbb{B}(\mathbf{u} - \mathbf{u}_{\infty}) \end{cases} \tag{2}$$

where $\mathbf{u}$ is the velocity, p the pressure and t the time. The density and the dynamic viscosity are respectively ρ and μ whereas the subscript sm denotes a sub-mesh contribution and is provided by a turbulence model. Finally, the last term in the r.h.s. of Eq. (2) is a Darcy like penalty term [23] used to deal with the boundary conditions as well as the immersed objects. $\mathbb{B}$ is here a diagonal tensor whose coefficients are zero in the interior fluid domain, leading to the classical Navier-Stokes equations, and tend to infinity at boundaries and in solid inclusions. This latter choice allows to locally enforce the fluid velocity to the prescribed one, $\mathbf{u}_{\infty}$.

In addition, an advection diffusion equation is used to deal with the transport of the passive tracer gas (acetone) concentration C:

$$\frac{\partial C}{\partial t} + \nabla \cdot (\mathbf{u}C) = \nabla \cdot ((\alpha + \alpha_{sm}) \nabla C) \tag{3}$$

where the molecular diffusion coefficient for the concentration is α and α_{sm} is once again the sub-mesh contribution provided by a proper model.

Leading a Direct Numerical Simulation (DNS) of the problem, i.e. $\mu_{sm} = \alpha_{sm} = 0$, would allow for an unsteady modelling of the problem. In this turbulent modelling strategy, $\mathbf{u}$, p and C are the real unsteady variables of the flow. However, this approach is often too expensive in computational time and even impossible to deal with if the Reynolds number of the flow is too large. An unsteady LES turbulence modelling is thus used in this work. It relies on the filtering of the flow and concentration variables as follows:

$$\mathbf{u} = \widehat{\mathbf{u}} + \mathbf{u}', \quad p = \widehat{p} + p' \quad \text{and} \quad C = \widehat{C} + C' \tag{4}$$

where $\widehat{\bullet}$ is the filtered component of the real variable and $\bullet'$ the sub-filter or sub-mesh contribution. Under the LES framework, $\bullet$ variables in Eqs.(2)-(3) are actually the filtered variables of the problem, i.e. $\mathbf{u} = \widehat{\mathbf{u}}$, $p = \widehat{p}$ and $C = \widehat{C}$. To close the motion equation Eq. (2), the functional Wall-Adapting Local Eddy-viscosity (WALE) model proposed by [33, 39], designed for its adapted behavior in the presence of walls, was selected among other LES models based on a comparative study on similar configurations.

Concerning the transport equation (Eq. (3)) for the passive pollutant concentration C, the sub-mesh diffusion coefficient α_{sm} is then expressed according to a classical turbulent Schmidt analogy based on the previous models for the sub-mesh turbulent viscosity as $\alpha_{sm} = \mu_{sm}/(\rho Sc_t)$ with the turbulent Schmidt number Sc_t chosen equal to 1 for the air medium present in our turbulent motion.

2.3.2. Boundary conditions

The boundary conditions enforcing dynamics and pollutant concentrations are the following:

- For the dynamic part, Dirichlet boundary conditions are prescribed on all walls, at domain boundaries or at immersed fixed objects, such that $\widehat{\mathbf{u}} = \mathbf{0}$. At inlets and outlets, flat velocity profiles are imposed such

that the value of the normal component $\widehat{\mathbf{u}} \cdot \mathbf{n}$ is chosen according to the prescribed velocities and mass flow rates given in Table 1. The mass flow rate of the additional exhaust is adapted to satisfy the mass conservation at the discrete level.

- Concerning passive pollutant concentration, no flux boundary conditions are imposed on both walls and outlets such that $\nabla \widehat{C} \cdot \mathbf{n} = 0$. At the inlets, a constant value $\widehat{C} = C_{in}$ is prescribed.

2.4. Codes and Numerical methods

The present work has been investigated with the homemade code Fugu, developed at MSME laboratory. The conservation equations (2) are discretized in space with finite volumes and centered schemes on staggered meshes. An implicit time discretization is used for all terms. The nonlinear inertial term of the momentum equation is semi-linearized and formally reads $\nabla \cdot (\widehat{\mathbf{u}}^{\star} \otimes \widehat{\mathbf{u}}^{n+1})$, with $\widehat{\mathbf{u}}^{n+1}$ and $\widehat{\mathbf{u}}^{\star}$ the velocity field at time iteration $n+1$ and linearly extrapolated from previous times step. With a constant time step, $\widehat{\mathbf{u}}^{\star} = 2\widehat{\mathbf{u}}^{n} - \widehat{\mathbf{u}}^{n-1}$. The coupling between pressure and velocity fields, under the incompressible assumption, relies on a time-splitting method, being the implicit formulation of the projection method originally proposed by [17].

In the same framework, Eq. (3) for passive scalar pollutant concentration is discretized with a centered scheme for the diffusion term. Concerning the advection term, as the cell Péclet number can be high, the use of standard centered schemes can be assumed to be inappropriate and introduce spurious non-physical oscillations. Multiple tests on a similar simplified configuration showed that high order schemes (like QUICK or WENO) do not improve significantly the solution with respect to the classical hybrid scheme used in the present work.

Combined with a MPI based domain decomposition approach, BiCGStab(2) solver with iLU preconditionner is used to solve linear systems where relative residuals are set to 10^{-6} for both prediction and projection steps of the time-splitting method as well as for the concentration equation. Computations are carried out on supercomputers on hundreds (up to 720) processors. A convergence study has been carried out on grids from 3 to 25 million cells and allowed to isolate a minimum cell size requirement of about 1 cm in the interest area, i.e. nearby the open cavity. To satisfy this constraint, the retained staggered irregular mesh is made of about 11 million cells, with a number

of control volume in each space direction respectively given by $N_x = 320$, $N_y = 220$ and $N_z = 160$.

Time uncorrelated states required to define the initial state before the departure of the moving object are obtained using a similar procedure to that described in Sec. 2.2.5. After an average flow establishment time, pollutant is injected during 300 seconds and the time step Δt is fixed to 1×10^{-2} s. The moving obstacle is then set in motion and variables of interest are recorded over 40 seconds of physical time. The same process is repeated 20 times.

2.5. Proper Orthogonal Decomposition of velocity snapshots

A Proper Orthogonal Decomposition (POD) of phase-averaged instantaneous velocity fields (snapshots) is used to compare the dynamical content of PIV measurements and LES modelling, in addition to traditional point-to-point velocity comparisons. This decomposition was introduced in the field of fluid mechanics by [25]. It is retained here for its ability at summarizing in the most compact form most of the energy content of the flows, hence facilitating the comparison of the large generated datasets. We adapt here the "snapshot POD" of [44]. In brief, the time varying 2D field of 3 velocity components at the cavity open surface are first reshaped in a 2-dimensional space-time data matrix D with positions and components along the first dimension and time along the second dimension. Hence, if we denote $u_{k_{i,j}}$ the k^{th} velocity component at measurement point i and time-step j, we have $u_{k_{i,j}} = D_{i+(k-1)N,j}$, where N is the number of measurement points. An orthogonal decomposition of D in the form $D = \Phi_P \Sigma_P \Psi_P{}^\intercal$ is then looked for, where Σ_P is the amplitude matrix of each mode (diagonal), Φ_P is the basis of spatial modes and Ψ_P is the temporal basis. To do so, the temporal auto-correlation matrix of the dataset is computed as $K = D^\intercal D$, and K is diagonalized as $K = \Psi_P \Lambda_P \Psi_P{}^\intercal$. Then the amplitude matrix is obtained by $\Sigma_P = \sqrt{\Lambda_P}$ and the projection is completed to yield the spatial basis matrix with $\Phi_P = D\Psi_P \Sigma_P^{-1}$. Note that the POD is performed from the diagonalization of the temporal auto-correlation matrix and not from that of the spatial auto-correlation matrix because the number of time steps is largely inferior to that of PIV measurement points. The truncation of the POD decomposition allows reconstructing an estimate (or a compression) of the dataset based on a reduced number of modes, i.e. an estimate of D with the first r modes simply reads : $\widetilde{D}^r = \widetilde{\Phi_P}^r \widetilde{\Sigma_P}^r \widetilde{\Psi_P}^{r\intercal}$, where $\widetilde{}^r$ denotes a truncation of matrices to keep only the first r modes (i.e. first r basis vectors

and amplitudes). According to the Eckart–Young–Mirsky theorem, the L_2 norm of the reconstruction error is easy to appreciate since it is equal to the amplitude of the next discarded mode, i.e. $\|D - \widetilde{D}^r\|_2 = \Sigma_{P_{r+1}}$.

3. Results

3.1. Similarity of modelled and experimental initial condition

Before examining results for the time dependent-problem, the similarity of experimental and modelled initial conditions is evaluated by comparing the mean τ_p values measured in steady-state initial conditions with corresponding CFD predictions. This comparison is proposed in figure 3. An overview of the mesh dependency of the simulation result for the initial steady-state flow is also shown on the figure, through CFD error bars that correspond to the extrema of variations of predicted τ_p for 4 discretizations of space with increased resolution, $192\times131\times102$, $224\times153\times119$, $256\times174\times136$ and $320\times220\times160$. CFD and experimental τ_p values are found close to each other, with 7.7% of difference in average, except perhaps for PID #232 which exhibits 23% of difference between measurement and CFD. These results suggest that the initial flow condition is satisfactorily retrieved by the CFD model. The mesh-dependency of τ_p appears small for the tested meshes (in average 3% of variation with the mesh resolution, and maximum of 8.7% for PID #222), which suggests that the coarsest mesh used is already sufficient to provide mesh-converged values of τ_p for the initial steady-state flow. As explained in section 2.4, the finest mesh was however retained for the subsequent time-dependent problem.

3.2. Time resolved tracer gas concentrations on the open surface

As exposed in paragraph 2.2.3, CFD results for the tracer gas concentration are time-filtered with the estimated PID model of equation 1 before being compared to PID measurements. Phase-averaged time series of measured and filtered simulated concentration signals are shown in figure 4, for the 4 measurement points on the open surface of the cavity sketched in supplementary figure S.**??**. The envelope for the CFD result correspond to the standard deviation across repetitions, with a coverage factor of 2 (assumed level of confidence of 95%). The envelope for the measurement result correspond to the expanded uncertainty on $\left\langle \widetilde{C} \right\rangle$ with identical coverage factor. Corresponding standard uncertainties are computed as exposed in supplementary section S.**??**. Peaks of pollutant concentrations appear on the open

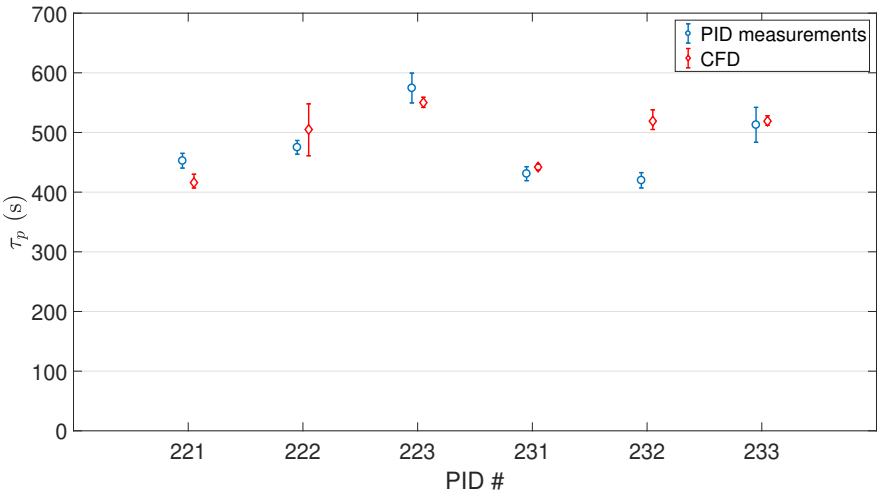

Figure 3: Measured and computed mean τ_p at the PIDs. Experimental error bars correspond to expanded uncertainties and CFD error bars correspond to extrema between computational grids

surface of the cavity after the obstacle has passed, and peaks are logically seen first on the right side of the surface (relative time delay of about 1.4 s between bottom-right and left PIDs) since the obstacle motion is from right to left. No significant concentration peak is found for the top right PID. Qualitatively, modelling results compare well with experimental results, simulations showing concentration peaks for the same sensors than in experiments, with the same temporal organization (with 1 to 1.4 s of time delay between bottom-right and left PIDs). Quantitatively, the orders of magnitude of the concentration peaks are retrieved by the simulations, which however overestimate the intensity of the peaks by 50 to 170 % depending on the sensor. CFD peaks appear sharper and happen earlier in simulations than in experiments (between 0.47 and 0.71 s of time delay according to peaks of signals cross-correlations, i.e. between 16 and 25% of T_T), suggesting a dampening phenomenon not taken into account in simulations.

3.3. Instantaneous velocities on the open surface

A comparison of the measured and simulated phase-averaged instantaneous air velocities on the open surface of the cavity is proposed in figure 5, for a grid of 3×2 points uniformly distributed on the open surface. A side-by-side animation of the measured and simulated velocity field on the

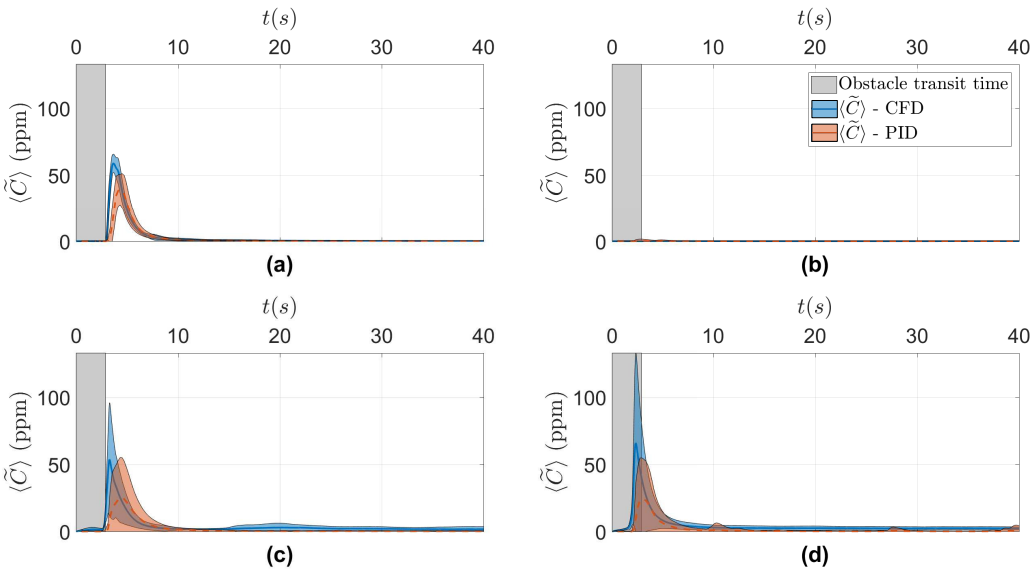

Figure 4: Time series of concentration at the open surface of the cavity : (a,b,c,d) correspond respectively to top-left, top-right, bottom-left and bottom-right sensors

open surface of the cavity is provided as supplementary material, together with supplementary videos highlighting the interaction of the moving obstacle with the velocity and concentration fields. Only the main velocity component $\langle v \rangle$, normal to the open surface of the cavity, is shown in figure 5. CFD and measurement error bars correspond to 95% confidence intervals on phase averages. The contribution of PIV uncertainties is not shown since it is not precisely known, but additional uncertainty of 1.6 to 9.6% is expected as explained in 2.2.3. The CFD simulation is found able to reproduce the dynamics of the breach of the containment barrier induced by the wake of the moving obstacle. This breach is characterised by a temporary inversion of the velocity component normal to the open surface, followed by a return to the initial steady-state of the flow where the normal velocity component is very uniform over the open surface and equals to its set bulk value of 0.4 m.s^{-1}.

The flow perturbation appears earlier in simulations than in experiments (in average 0.6 s of time delay according to peaks of signals cross-correlations, not shown here), similarly to the trend observed for concentration signals. Quantitatively, if we cancel out this time lag by forcing signals synchronization, the absolute difference between modelled and measured velocity

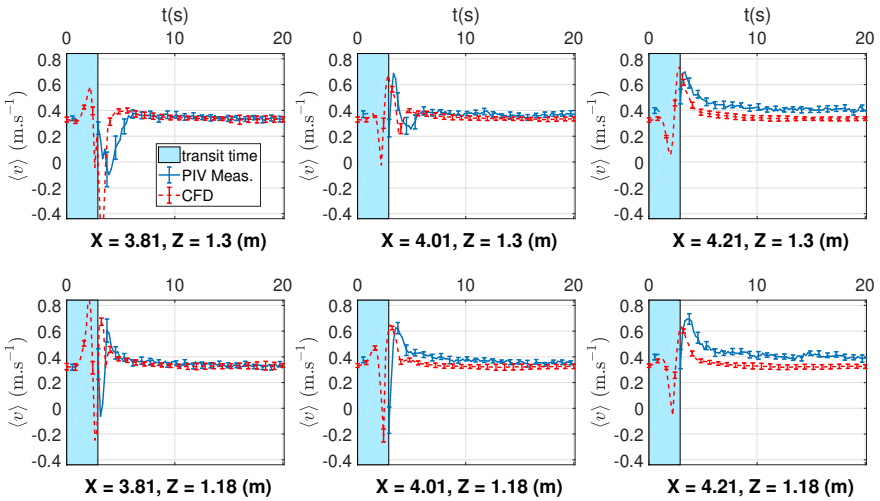

Figure 5: Time series of the normal component of air velocity at the open surface of the cavity

components can be summarized by the boxplot of figure 6, for all points of the open surface and for the whole experimental time. Experimental to simulation velocity differences are expressed in percent of the obstacle nominal velocity U_{obj}. Boxes delimit the region between the 25th and 75th percentiles, the middle line marks the median and whiskers embrace 99% of the values. The distributions of figure 6 indicate that the mean absolute difference between measured and modelled velocities is of respectively 5%, 8% and 6% for the normal (v), and span wise (u, w) components, while 95% of points present an absolute difference below respectively 13%, 18% and 15% for the normal (v), and span wise (u, w) components. Largest discrepancies are found for the u component which is aligned with the direction of the obstacle motion. While these results might be considered rather quite acceptable for this complex setup, the POD analysis may better illustrate the similarity between the model and the experience.

3.4. POD modes comparison

The snapshot-POD exposed previously is applied to the 3 instantaneous phase-averaged velocity components at the open surface of the cavity, at the PIV measurement points and timestamps. Simulation data are extracted to correspond to identical times and positions, and only times after $t = 2.92$ s are

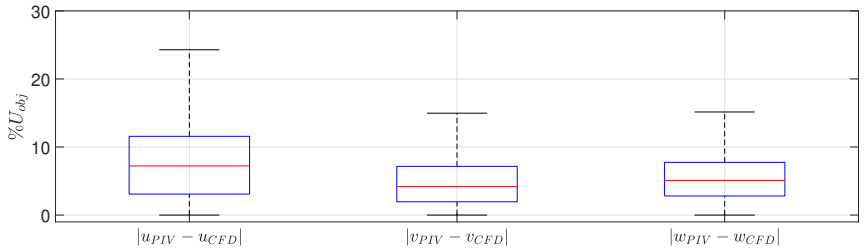

Figure 6: Distributions of absolute differences between predicted and measured velocities on the cavity open surface after forced time-synchronization

treated since the PIV dataset present gaps due to obstacle optical obstruction before.

The first 3 modes of the POD represent 98% of the energy content of the dataset and are thus representative of the essential features of the flow. These modes are detailed in figures 7 to 9. These figures show on their left side the spatial structure Φ_P of modes 1 to 3, vectors representing the in-plane components while the out-of-plane component is represented by the colormap. On the right of figures 7 to 9 the corresponding temporal structure Ψ_P is plotted. The energy content of each mode is indicated above each Φ_P field.

The first two POD modes of PIV and CFD velocities, which represent respectively 93% and 96% of energy content, appear very similar in magnitude and direction of their spatial structure. Their temporal structure is also similar, but exhibit a time-delay of about $0.4-0.6$ s between simulations and experiments, as already visible while comparing the time series of air velocity and tracer gas concentrations. POD mode 3 shows more differences between PIV and simulations but represents already a marginal fraction of kinetic energy (4.6% for PIV and 2.1% for CFD). Temporal structures for mode 3 are still very similar, with still a time delay between CFD and PIV, but the spatial structures differ more, although similarities are obvious. We may conclude from the comparison of the first two modes that the flow dynamics predicted by CFD is essentially very similar to experimental observations, except for the slight time delay.

CFD and PIV PODs can be compared here because they rely on the same spatial and temporal discretization of velocities, with a time synchronization based on the start of the moving obstacle. Also the contribution of the random turbulent content of velocities is largely eliminated by the

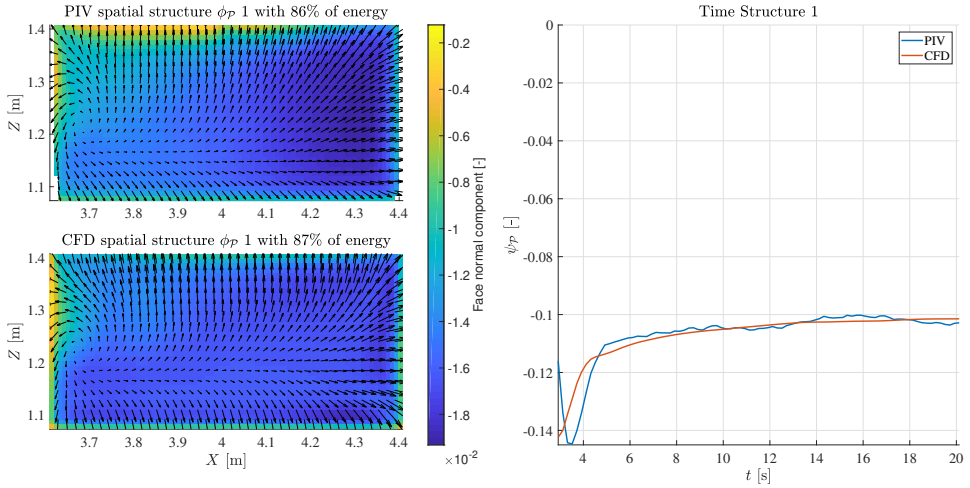

(a) (b)

Figure 7: Mode 1 spatial (a) and temporal (b) structures

phase-averaging process that leaves only the mean unsteady flow perturbation induced by the wake of the obstacle. However, beyond the comparison of measurements and simulation data, the significance of the present POD from a physical point of view is not straightforward. We may observe that mode 1 is characterized by a rather uniform out-of-plane spatial component with a permanent existence in time ($\Psi_P 1$ remains between -0.1 and -0.14 in figure 7) : clearly, mode 1 is then essentially associated with the undisturbed steady flow at the open surface of the cavity, which enforces the containment of the aerodynamic containment barrier in steady-state. In contrast, mode 2 exhibits a strong localized out-of-plane component $\Phi_P 2$ in the opposite direction to $\Phi_P 1$, in the top left corner of the open surface. This structure is associated with a more evanescent existence in time (approx. between 2.9 and 5.5 s). Clearly mode 2 can then be associated with the temporary containment breach induced by the wake of the moving obstacle.

3.5. Influence of initial turbulent state in the room over pollutant leaks

Results presented so far correspond to phase-averages of concentrations and velocities over repetitions of the experiment. The variability of results between repetitions is noticeable, as shown by error bars over times series of velocity and concentrations in figures 4 and 5 that essentially correspond

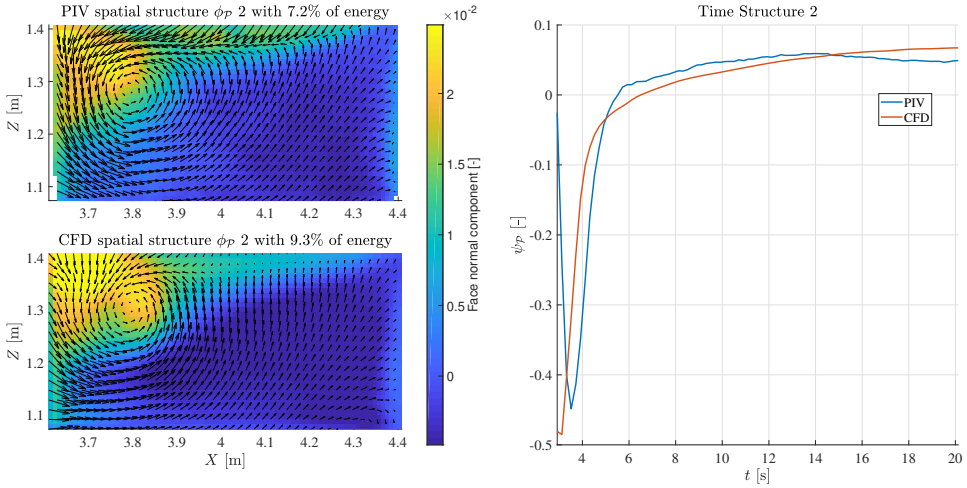

(a) (b)

Figure 8: Mode 2 spatial (a) and temporal (b) structures

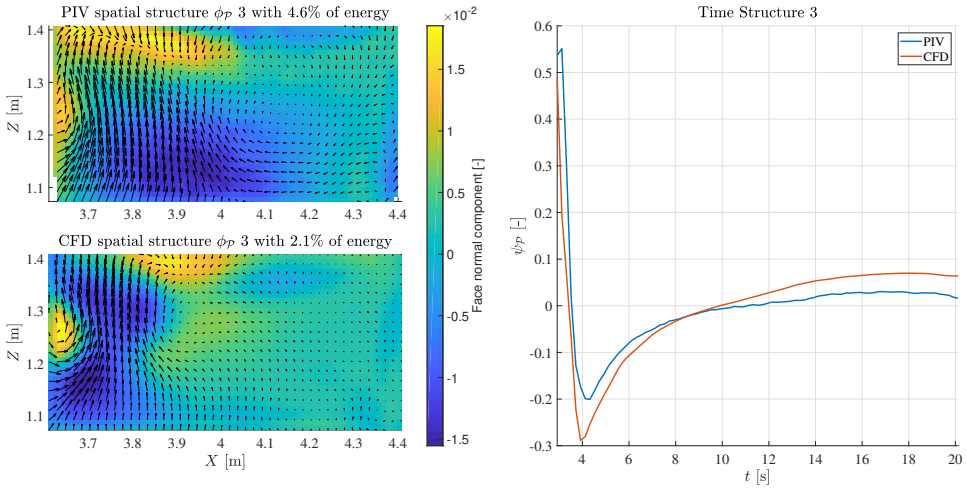

(a) (b)

Figure 9: Mode 3 spatial (a) and temporal (b) structures

to 95% confidence interval on phase averages. If the origin of repeatability errors is difficult to isolate experimentally, it is in contrast easy to identify in CFD simulations. Successive time-dependent CFD simulations are indeed performed with identical steady boundary conditions and initial mean flow: the only differences between repetitions rely then on the turbulent component of the initial steady-state flow in the room.

These differences lead to variations, between repetitions, of the predicted peak height of pollutant concentration at the open surface of the cavity that can be as high as the phase-averaged peak height. This is shown in figure 10 which plots the envelope of variations and the phase average of acetone concentrations C for the measurement points on the open surface of the cavity, such as predicted by the CFD modelling. Note that, for this figure, no PID filter model is employed since this plot is not dedicated to experimental comparison.

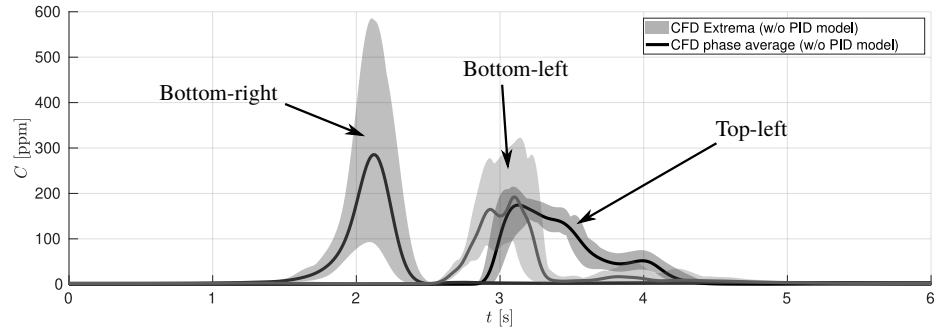

Figure 10: Variations between repetitions and phase-average of CFD-predicted concentration signals at the open surface

These modelling results thus lead to an observation of primary importance that has not been illustrated so far to our knowledge: the consequences of a draft, such as caused by a moving obstacle, on the perturbation of an aerodynamic containment barrier contain an intrinsically variable part which depends on the state of turbulence of the surrounding air, prior to the draft. Thus, depending on that initial state of turbulence, for the same situation an identical draft may cause a noticeably different pattern of air velocities inversion at the open surface of a ventilated enclosure, associated to different pollutant outbursts, leading to variable exposure of operators nearby.

4. Discussion

If CFD modelling agrees qualitatively well with experimental data, there remains quantitatively noticeable gaps between measured and simulated concentration signals and velocities. These gaps can be explained by both experimental and numerical issues.

One of the possible major differences between the experimental and numerical cases is the initial condition of the flow, i.e. the air velocity field at the time when the obstacle starts moving. Many efforts have been made to limit the role of uncontrolled natural convection on the initial steady-state flow, but the analysis of Richardson numbers provided in the material and methods section shows that uncontrolled natural convection cannot be excluded. Natural convection may have affected initial conditions either with a systematic or random bias, depending on the occurrence of thermal disturbances. The repeatability uncertainties on mean ages of air in steady-state (table 2) indicate that the initial flow was quite repeatable, which minimizes the role of a random bias, but a systematic difference with respect to simulated condition induced by a permanent temperature gradient is still possible. For the time dependent problem, the effect of initial condition differences could then be amplified by the dynamics of the system, as shown by the sensitivity of results with respect to initial conditions in section 3.5.

In addition to differences of initial conditions, experiments and modelling present unavoidable differences of boundary conditions. These differences are first geometrical: the real geometry was made as close as possible to an assembly of rectangular blocks, but some simplifications were still required for modelling. To these simplifications, a rasterization of objects (to within 1 cm) induced by the discretization process and by the penalty method adds. Besides rasterization effect, the penalty method employed does not take into account the development of a boundary layer along the walls of the moving object, which results in a necessarily approximate wake flow. As regards air velocity profiles and flow rates at inlet and outlets, the venturi-measured flow rates showed up to respectively 1.4%, 6.3% and 3.4% of uncertainty at the inlet, cavity outlet and secondary outlet respectively: these uncertainties are not taken into account in simulations. The velocity profile at the air diffuser provided to the CFD model and measured by the ultrasonic anemometer is also subject to measurement uncertainties, although the surface integral of this profile falls within 1.7% of the reference flow rate measured by the venturi flow meter, as shown in supplementary S.**??**. There also exist uncertainties

on the motion of the moving object.

Besides these differences of input parameters between CFD and experiment, we must also stress the role of measurement uncertainties while characterizing experimentally or numerically the breach of the containment barrier induced by the wake of the obstacle. Regarding PIV measurements of the instantaneous velocity field, the comparison of the venturi-measured flow rate with the surface integral of the PIV velocity component v normal to the open surface of the cavity indicates that PIV systematically underestimates v by 6.8 to 9.8% in average. The PIV local instantaneous uncertainty on v was not derived, reason why error bars of figure 5 do not take into account this contribution. However, if we assume that the PIV measurement error on v is comparable to that on its surface integral, PIV measurements of v appear closer to CFD predictions. Regarding acetone instantaneous concentration measurements, one of the most important weaknesses is the intrusiveness of the employed detectors, associated to a stopping point of the flow on the detectors that prevents vapors from reaching the sensor except by diffusion, whence an increased response time. The intrinsic quality of the sensors also undoubtedly affected measurements. Efforts were made to in-situ calibrate the dynamic response of PIDs to make CFD predictions comparable to measurements. However, measurements remain affected by the imperfect and variable response of PIDs. Thus, no perfect sensor model was found for PIDs, as shown in S.**??**, since the PIDs exhibit a sensitivity to history and a lack of repeatability of their long term response. Anyway, the PID dynamic modelling error concerns essentially the response to time-scales longer than 3.5 s, that is beyond the lifetime of the observed concentration outbursts. The lack of repeatability of PID response to identical concentration steps is also cancelled by the phase averaging process. Overall, the comparison of measured and CFD predicted concentrations suggests that the dynamics of gas transfer at the open surface of the cavity is reasonably well captured by both CFD and PIDs, even if PIDs present an actual 3 db cut-off time-scale of about 1.4 s which is quite long compared to the time-scale of the draft T_T. Overall, despite the exposed numerical and experimental issues, CFD results appear validated by experimental measurements, within the evoked uncertainties.

5. Conclusion

In this paper, we studied both experimentally and numerically the flow and contaminant transfer at the interface of an aerodynamic containment barrier submitted to the transient wake of a moving obstacle. The main aim was to evaluate the ability of a penalized LES approach to predict the corresponding flow and contaminant dynamics, in the context of scale 1 laboratory environments, while providing a general validation case for CFD modelling of similar situations. Time-resolved 2D-3C air velocity PIV measurements at the open surface of a ventilated enclosure were used in that purpose, together with time-resolved concentration measurements of acetone vapors, that were initially released from the bottom surface of the enclosure.

In the studied case, the initial steady-state flow, characterized by a uniform mean velocity field at the open face of the ventilated cavity that prevents acetone vapor from escaping, is temporarily disturbed by the mass of fluid displaced by the moving obstacle and then by the wake behind it. This results in a simultaneous local increase of the inward velocity, associated to a reversal of the flow direction on a fraction of the open surface accompanied by a puff of acetone. The inward flow reaches back its initial uniform state shortly after the obstacle stopped moving. In that context, penalised-LES simulation was found able to reproduce well the dynamics of the containment breach, both in terms of spatial and temporal structures of the transient flow obtained by POD, and in terms of magnitude of the instantaneous velocity components and acetone concentration at the open face of the cavity. The flow perturbation is found to appear earlier in simulations than in experiments, with a time delay of approx. 0.6 s (i.e. 21% of T_T), both as regards the modifications of velocities and concentrations. Disregarding this time-delay, simulation and measurements are quantitatively in accordance considering the experimental uncertainties, with a mean absolute difference between measured and modelled velocities of less than 8% of the obstacle nominal velocity U_{obj}, and with 95% of points presenting an experimental to simulation absolute velocity difference of less than 18% of U_{obj}. Experimental concentration peaks occurring during the containment breach are less well retrieved quantitatively by simulations, with up to 45 ppm of difference for an average experimental peak height of 30 ppm, but this is probably largely attributable to the difficulty of measuring non-intrusively such evanescent (< 2 s) and diluted (< 100 ppm) concentrations of acetone

with the employed photo-ionization detectors.

Beyond the mere validation of its CFD modelling, the considered case reveals the sensitivity of the containment breach with respect to the initial turbulent state in the room, as a consequence of the well known chaotic behaviour of the underlying Navier-Stokes equations for such Reynolds numbers. CFD results show that the intensity of pollutant puffs escaping the ventilated enclosure is intrinsically very variable (up to 100% variation is observed here), for identical ventilation conditions but variable initial turbulent state in the room. This rather expected but unprecedented (to our knowledge) observation, brings an important consequence and some prospects in the field of risk management measures. First, the consequences of a draft on the short-term exposure of workers handling chemicals in such ventilated enclosures is highly variable, in connection to the turbulence existing in the room prior to the draft: these consequences must hence be evaluated statistically, both when an experimental or numerical approach is used. Second, a lead for future research would be to try correlating some moments characterizing initial turbulence in the room to puffs intensities, in order to highlight the origin of puffs amplification and perhaps find remediation solutions to lower the intensity of puffs and enhance workers protection.

To make present work as useful as possible for the community, data including detailed airflow boundary conditions were set up to form a reference case for the evaluation of CFD models and are made available as supplementary material.

6. Acknowledgements

We are grateful for access to the computational facilities of the French CINES (National computing center for higher education) and TGCC, notably Irene-Rome, granted by GENCI under project numbers A0112b06115 and A0092B06115.

References

[1] Al Assaad, D., Ghali, K., Ghaddar, N., 2019a. Effect of flow disturbance induced by walking on the performance of personalized ventilation coupled with mixing ventilation. Building and Environment 160, 106217.

[2] Al Assaad, D., Ghali, K., Ghaddar, N., 2019b. Particles dispersion due to human prostration cycle and ventilation system in a prayer room. Building and Environment 150, 44–59.

[3] Bhattacharya, A., Pantelic, J., Ghahramani, A., Mousavi, E.S., 2021. Three-dimensional analysis of the effect of human movement on indoor airflow patterns. Indoor Air 31, 587–601.

[4] Bjørn, E., Nielsen, P.V., 2002. Dispersal of exhaled air and personal exposure in displacement ventilated rooms. Indoor air 12, 147–164.

[5] Brohus, H., Balling, K., Jeppesen, D., 2006. Influence of movements on contaminant transport in an operating room. Indoor air 16, 356–372.

[6] Brohus, H., Hyldig, M., Kamper, S., Vachek, U.M., 2008. Influence of persons' movements on ventilation effectiveness, in: Proceedings of Indoor Air 2008: The 11th International Conference on Indoor Air Quality and Climate, Copenhagen, Denmark, 17-22 August, 2008, Technical University of Denmark (DTU).

[7] CEN, 2019. Fume cupboards - Part 3: Type test methods. Standard. European Committee for Standardization. Brussels.

[8] Chang, L., Tu, S., Ye, W., Zhang, X., 2017. Dynamic simulation of contaminant inleakage produced by human walking into control room. International Journal of Heat and Mass Transfer 113, 1179–1188.

[9] Chang, L., Zhang, X., Wang, S., Gao, J., 2016. Control room contaminant inleakage produced by door opening and closing: Dynamic simulation and experiments. Building and environment 98, 11–20.

[10] Choi, J.I., Edwards, J.R., 2012. Large-eddy simulation of human-induced contaminant transport in room compartments. Indoor air 22, 77–87.

[11] Choi, J.I., Edwards, J.R., Rosati, J.A., Eisner, A.D., 2012. Large eddy simulation of particle re-suspension during a footstep. Aerosol Science and Technology 46, 767–780.

[12] Chow, T.T., Wang, J., 2012. Dynamic simulation on impact of surgeon bending movement on bacteria-carrying particles distribution in operating theatre. Building and environment 57, 68–80.

[13] Drmac, Z., Gugercin, S., Beattie, C., 2015. Quadrature-based vector fitting for discretized h_2 approximation. SIAM Journal on Scientific Computing 37, A625–A652.

[14] Eames, I., Shoaib, D., Klettner, C., Taban, V., 2009. Movement of airborne contaminants in a hospital isolation room. Journal of the Royal Society Interface 6, S757–S766.

[15] Edge, B.A., Paterson, E.G., Settles, G.S., 2005. Computational study of the wake and contaminant transport of a walking human. Journal of Fluids Engineering 127, 967–977. URL: https://doi.org/10.1115/1.2013291, doi:10.1115/1.2013291, arXiv:https://asmedigitalcollection.asme.org/fluidsengineering/article-pdf/127

[16] Faghri, A., Zhang, Y., 2006. Transport phenomena in multiphase systems. Elsevier.

[17] Goda, K., 1979. A multistep technique with implicit difference schemes for calculating two-or three-dimensional cavity flows. Journal of Computational Physics 30, 76–95.

[18] Goldasteh, I., Tian, Y., Ahmadi, G., Ferro, A.R., 2014. Human induced flow field and resultant particle resuspension and transport during gait cycle. Building and Environment 77, 101–109.

[19] Hambraeus, A., Bengtsson, S., Laurell, G., 1977. Bacterial contamination in a modern operating suite. 1. effect of ventilation on airborne bacteria and transfer of airborne particles. Epidemiology & Infection 79, 121–132.

[20] Han, Z., Weng, W., Huang, Q., 2014. Numerical and experimental investigation on the dynamic airflow of human movement in a full-scale cabin. HVAC&R Research 20, 444–457.

[21] Hang, J., Li, Y., Jin, R., 2014. The influence of human walking on the flow and airborne transmission in a six-bed isolation room: Tracer gas simulation. Building and Environment 77, 119–134.

[22] Johnson, A., Fletcher, B., 1996. The effect of operating conditions on fume cupboard containment. Safety science 24, 51–60.

[23] Khadra, K., Angot, P., Parneix, S., Caltagirone, J.P., 2000. Fictitious domain approach for numerical modelling of navier–stokes equations. International Journal for Numerical Methods in Fluids 34, 651–684.

[24] Knisely, C.W., 1990. Strouhal numbers of rectangular cylinders at incidence: a review and new data. Journal of fluids and structures 4, 371–393.

[25] Lumley, J.L., 1967. The structure of inhomogeneous turbulent flows. Atmospheric turbulence and radio wave propagation , 166–178.

[26] Luo, N., Weng, W., Xu, X., Fu, M., 2018. Human-walking-induced wake flow–piv experiments and cfd simulations. Indoor and Built Environment 27, 1069–1084.

[27] Lv, L., Zeng, L., Wu, Y., Gao, J., Xie, W., Cao, C., Chen, Y., Zhang, J., 2021. Effects of human walking on the capture efficiency of range hood in residential kitchen. Building and Environment 196, 107821.

[28] Matsumoto, H., Ohba, Y., 2004. The influence of a moving object on air distribution in displacement ventilated rooms. Journal of Asian Architecture and Building Engineering 3, 71–75.

[29] Mattsson, M., 1999. On the efficiency of displacement ventilation, with particular reference to the influence of human physical activity. Ph.D. thesis. Institutionen för byggd miljö.

[30] Mazumdar, S., Poussou, S.B., Lin, C.H., Isukapalli, S.S., Plesniak, M.W., Chen, Q., 2011. Impact of scaling and body movement on contaminant transport in airliner cabins. Atmospheric Environment 45, 6019–6028.

[31] Murakami, S., Zeng, J., Hayashi, T., 1999. Cfd analysis of wind environment around a human body. Journal of Wind Engineering and Industrial Aerodynamics 83, 393–408.

[32] NF EN ISO 5167-4, 2022. Measurement of fluid flow by means of pressure differential devices inserted in circular cross-section conduits running full - Part 4 : Venturi tubes. Standard. International Organization for Standardization. Geneva, CH.

[33] Nicoud, F., Ducros, F., 1999. Subgrid-scale stress modelling based on the square of the velocity gradient tensor. Flow, turbulence and Combustion 62, 183–200.

[34] Oberoi, R.C., Choi, J.I., Edwards, J.R., Rosati, J.A., Thornburg, J., Rodes, C.E., 2010. Human-induced particle re-suspension in a room. Aerosol Science and Technology 44, 216–229.

[35] Poussou, S.B., Mazumdar, S., Plesniak, M.W., Sojka, P.E., Chen, Q., 2010. Flow and contaminant transport in an airliner cabin induced by a moving body: Model experiments and cfd predictions. Atmospheric Environment 44, 2830–2839.

[36] Poussou, S.B., Plesniak, M.W., 2012. Vortex dynamics and scalar transport in the wake of a bluff body driven through a steady recirculating flow. Experiments in fluids 53, 747–763.

[37] Rouaud, O., Havet, M., Solliec, C., 2004. Influence of external perturbations on a minienvironment: experimental investigations. Building and Environment 39, 863–872.

[38] Saarinen, P.E., Kalliomäki, P., Tang, J.W., Koskela, H., 2015. Large eddy simulation of air escape through a hospital isolation room single hinged doorway—validation by using tracer gases and simulated smoke videos. PloS one 10, e0130667.

[39] Sagaut, P., 1998. Large Eddy Simulation for incompressible flows - An introduction. Springer Verlag.

[40] Sandberg, M., Sjöberg, M., 1983. The use of moments for assessing air quality in ventilated rooms. Building and environment 18, 181–197.

[41] Schuyler, G., 1990. Performance of fume hoods in simulated laboratory conditions. ASHRAE Transactions , 428–434.

[42] Shao, X., Hashimoto, K., Fang, L., Melikov, A.K., Naydenov, K.G., Rasmuseen, C., 2020. Experimental study of airborne particle transmission through the doorway of a cleanroom due to the movement of a person. Building and environment 183, 107205.

[43] Shih, Y.C., Chiu, C.C., Wang, O., 2007. Dynamic airflow simulation within an isolation room. Building and environment 42, 3194–3209.

[44] Sirovich, L., 1987. Turbulence and the dynamics of coherent structures. i. coherent structures. Quarterly of applied mathematics 45, 561–571.

[45] Tao, Y., Inthavong, K., Tu, J., 2017. Dynamic meshing modelling for particle resuspension caused by swinging manikin motion. Building and Environment 123, 529–542.

[46] Thatcher, T., Wilson, D., Wood, E., Craig, M., Sextro, R., 2004. Pollutant dispersion in a large indoor space: Part 1–scaled experiments using a water-filled model with occupants and furniture. Indoor Air 14, 258–271.

[47] Tseng, L.C., Huang, R.F., Chen, C.C., Chang, C.P., 2007. Effects of sash movement and walk-bys on aerodynamics and contaminant leakage of laboratory fume cupboards. Industrial health 45, 199–208.

[48] Villafruela, J., San José, J., Castro, F., Zarzuelo, A., 2016. Airflow patterns through a sliding door during opening and foot traffic in operating rooms. Building and Environment 109, 190–198.

[49] Wang, J., Chow, T.T., 2011. Numerical investigation of influence of human walking on dispersion and deposition of expiratory droplets in airborne infection isolation room. Building and Environment 46, 1993–2002.

[50] Wu, Y., Gao, N., 2014. The dynamics of the body motion induced wake flow and its effects on the contaminant dispersion. Building and environment 82, 63–74.

[51] Zhang, Z., Zhang, W., Zhai, Z.J., Chen, Q.Y., 2007. Evaluation of various turbulence models in predicting airflow and turbulence in enclosed environments by cfd: Part 2—comparison with experimental data from literature. Hvac&R Research 13, 871–886.

[52] Zhou, H., Zhong, K., Jia, H., Kang, Y., 2022. Analysis of the effects of dynamic mesh update method on simulating indoor airflow induced by moving objects. Building and Environment 212, 108782.